

## SUPPLEMENTARY INFORMATION

# Tug-of-War between Corrugation and Binding Energy: Revealing the Formation of Multiple Moiré Patterns on a Strongly Interacting Graphene-Metal System.

*Ana Martín-Recio,<sup>a</sup> Carlos Romero-Muñiz,<sup>b</sup> Antonio J. Martínez-Galera,<sup>a, c</sup> Pablo Pou,<sup>b, d</sup> Rubén Pérez,<sup>\*, b, d</sup> and José M. Gómez-Rodríguez,<sup>\*, a, d</sup>*

<sup>a</sup>Departamento de Física de la Materia Condensada, Universidad Autónoma de Madrid, E-28049, Madrid, Spain

<sup>b</sup>Departamento de Física Teórica de la Materia Condensada, Universidad Autónoma de Madrid, E-28049, Madrid, Spain

<sup>c</sup>Present address: II. Physikalisches Institut, Universität zu Köln, Zùlpicher Str. 77, 50937 Köln, Germany

<sup>d</sup>Condensed Matter Physics Center (IFIMAC), Universidad Autónoma de Madrid, E-28049, Madrid, Spain

## SUPPLEMENTARY INFORMATION CONTENTS

- 1.- Growth of graphene on Rh(111)
- 2.- Geometric model for the moiré patterns of G on Rh(111)
- 3.- Apparent corrugation of graphene on Rh(111) in STM experiments
- 4.- G/Rh(111) moiré patterns used in the DFT simulations
- 5.- Apparent corrugation of graphene on Rh(111) in STM simulations
- 6.- Complete list of references

## 1. Growth of graphene on Rh(111)

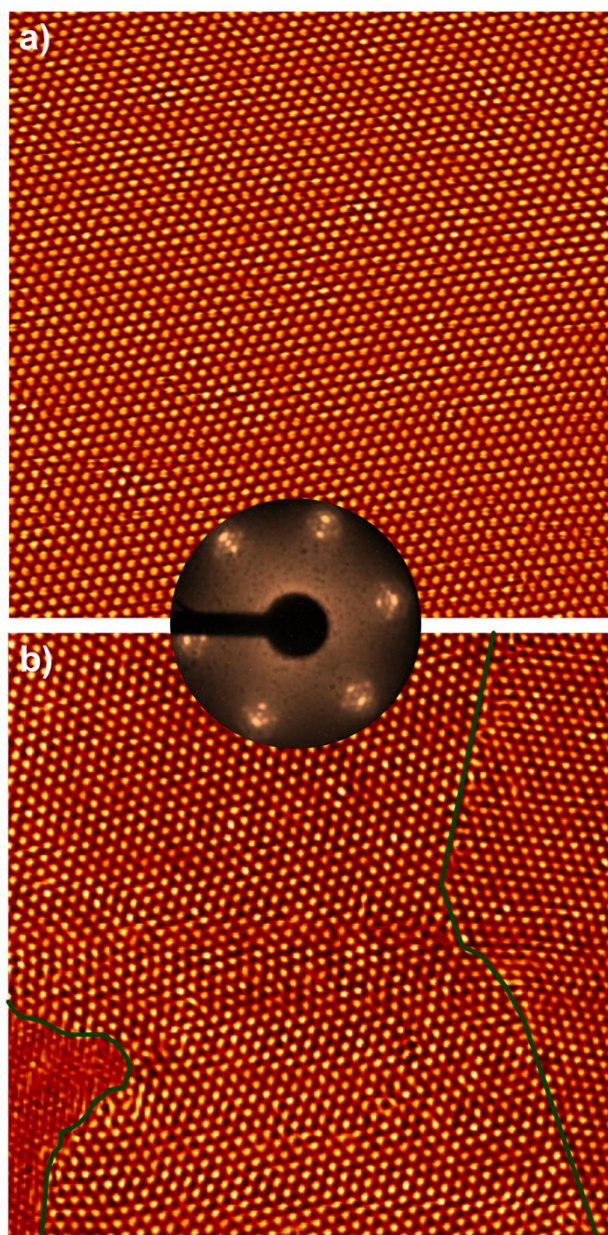


**Fig. S1.**  $120 \times 120 \text{ nm}^2$  STM images of 1ML graphene grown by UHV-CVD on Rh(111); (a) Only the largest moiré  $(12 \times 12)_G$  is observed in this area; tunnelling parameters,  $V_S = -0.3 \text{ V}$ ,  $I_T = 3.0 \text{ nA}$ ; inset: typical LEED pattern ( $E = 67 \text{ eV}$ ) observed after the sample preparation; (b) Another terrace where three different moirés are observed; tunnelling parameters,  $V_S = 0.8 \text{ V}$ ,  $I_T = 3.0 \text{ nA}$ .

In this section, the two graphene growth methods, UHV-CVD and bulk segregation, are illustrated. In both cases, the surfaces have been experimentally characterized by LEED and STM measurements. First, following the UHV-CVD method explained in the main

text, the graphene forms one monolayer. Fig. S1 shows the results of this preparation method; both are large scale STM images where the whole surface was covered with a well grown graphene layer. Fig. S1a shows a  $120 \times 120 \text{ nm}^2$  terrace where only the common orientation (0 degrees) of the graphene with respect to the Rh(111) has grown while in fig. S1b a similar terrace with three different graphene domains is observed. The inset of this figure shows the typical LEED pattern obtained through this UHV-CVD method. It is mainly visible the orientation of the 0 degree moiré which is consistent with the STM results being this rotational orientation the one that covers most part of the sample.

An example of the surfaces obtained with the carbon segregation method is shown in fig. S2. As observed in the STM image, the Rh(111) surface is covered by imperfect graphene patches in which some areas appear completely distorted. As the surface is not uniformly covered by well grown graphene, we discarded this growth method and focused on the first one. For this reason, the results shown in this work have been obtained following the UHV-CVD method.

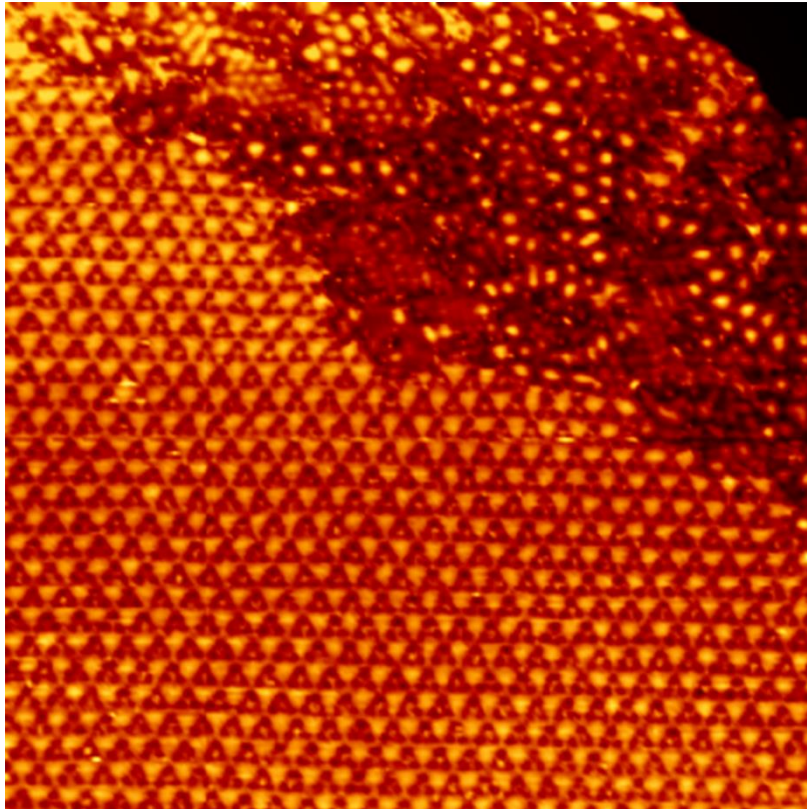


**Fig. S2.**  $73 \times 73 \text{ nm}^2$  STM image of an imperfect graphene patch grown by carbon segregation from the bulk on Rh(111); tunnelling parameters,  $V_S = 0.9 \text{ V}$ ,  $I_T = 1.6 \text{ nA}$ .

## 2. Geometric model for the moiré patterns of G on Rh(111).

Merino et al.<sup>18</sup> have developed a geometric model that relates the minimum values of the mismatch of all the possible superstructures with those experimentally found on graphene on Pt(111), Pd(111), Ir(111) and Ni(111). We have applied this simple model for our strongly coupled graphene on Rh(111) system.

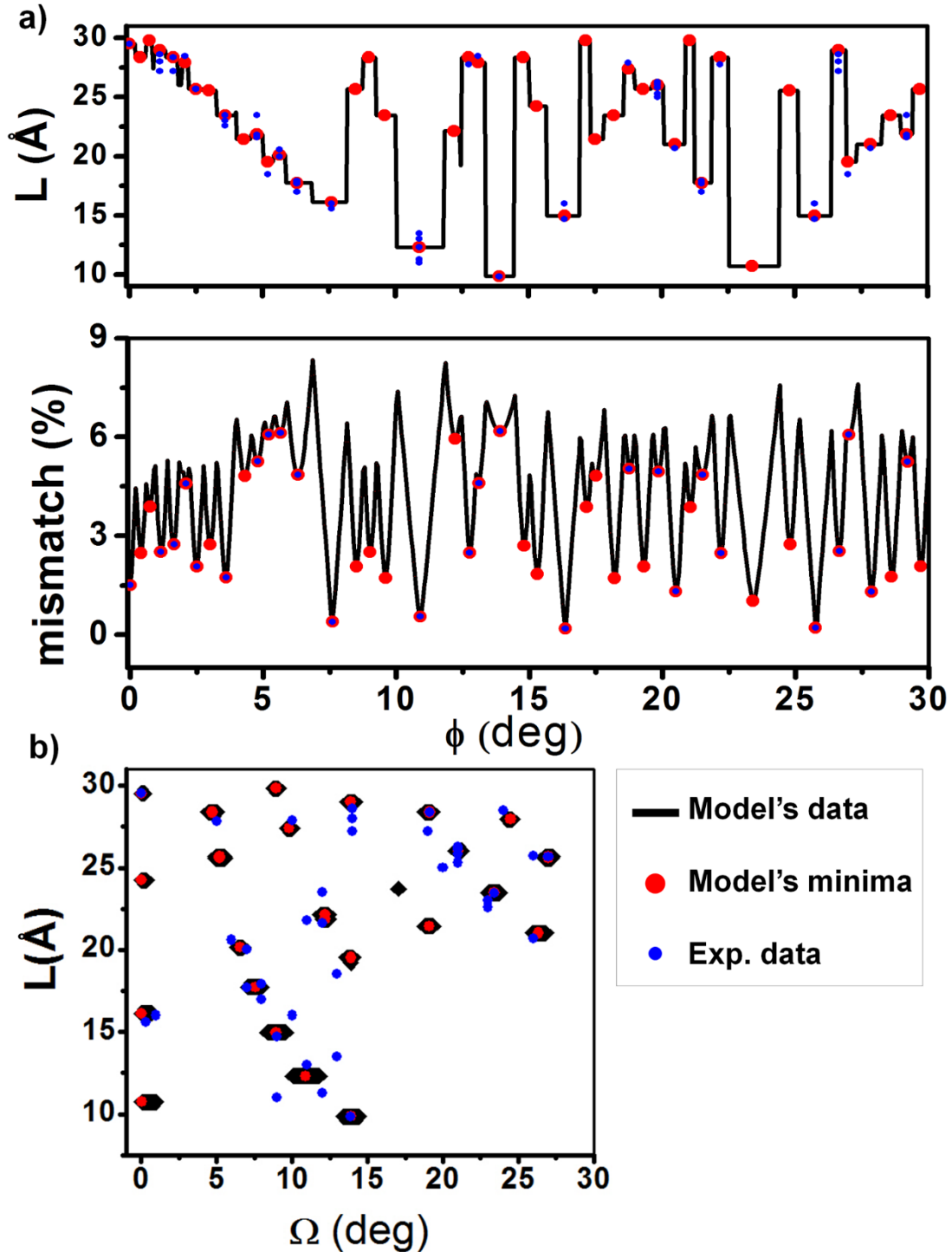


**Fig. S3.** Geometric model. (a) Plot of the lattice parameter ( $L$ ) and the absolute value of the mismatch of the possible moirés as a function of the angle between the graphene and

the Rh(111) arrays; (b) plot of the lattice parameter as a function of the angle between the moiré and the Rh(111). The black and red data have been obtained through the geometrical model being the red dots the mismatch minima values. The experimental data have been plotted with smaller blue dots.

By varying the crystallographic angle  $\phi$  between the metal layer and the graphene, this program obtains which superperiodicities (L) have the lowest mismatch of the graphene with the substrate. Every moiré forms also an angle with the hexagonal lattice of the metal named  $\Omega$ . So, every moiré structure is unequivocally defined by the two angles  $\phi$  and  $\Omega$ , its periodicity L and its mismatch. The results of these simple calculations are shown in fig. S3. Fig. S3a shows the periodicity and its corresponding mismatch as a function of every small rotation of the crystallographic angle  $\phi$  (black line). The red spots are those results with a relative mismatch minimum value and the blue dots the experimental data. Then, in fig. S3b the same results are also shown in a graph of the moiré periodicity as a function of the relative angle between the moiré and the metallic lattice. As one can see, the results of these simple calculations are in very good agreement with the superstructures found experimentally.

3. Apparent corrugation of graphene on Rh(111) in STM experiments.

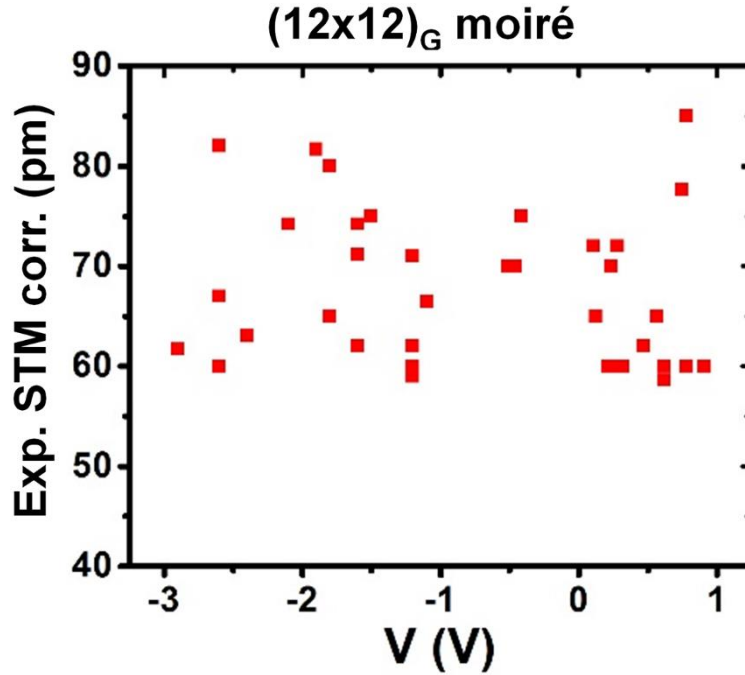


**Fig. S4.** Study of the  $(12 \times 12)_G$  moiré experimental corrugation variation with the bias voltage. There is no dependency of the apparent corrugation with the voltage.

A detailed study of the experimental apparent corrugation of the moiré patterns was carried out during this work. In order to see the variations of topographic images with the bias voltage (V), first the  $(12 \times 12)_G$  moiré was examined. Fig. S4 shows a plot, extracted from a large set of STM images, displaying the corrugation of this moiré as a function of V. There is no clear evidence of any dependency of the apparent corrugation with the voltage. The very slight variation of these values from ~60 to ~85 pm may be explained as due to different tip apex terminations on different experiments.

Then, also a study of the different moiré superstructures measured at different voltage ranges is shown in fig. S5. It is shown for four different ranges in four different colors, how the increasing trend of the apparent corrugation with the moiré lattice parameter is preserved independently of the voltage range.

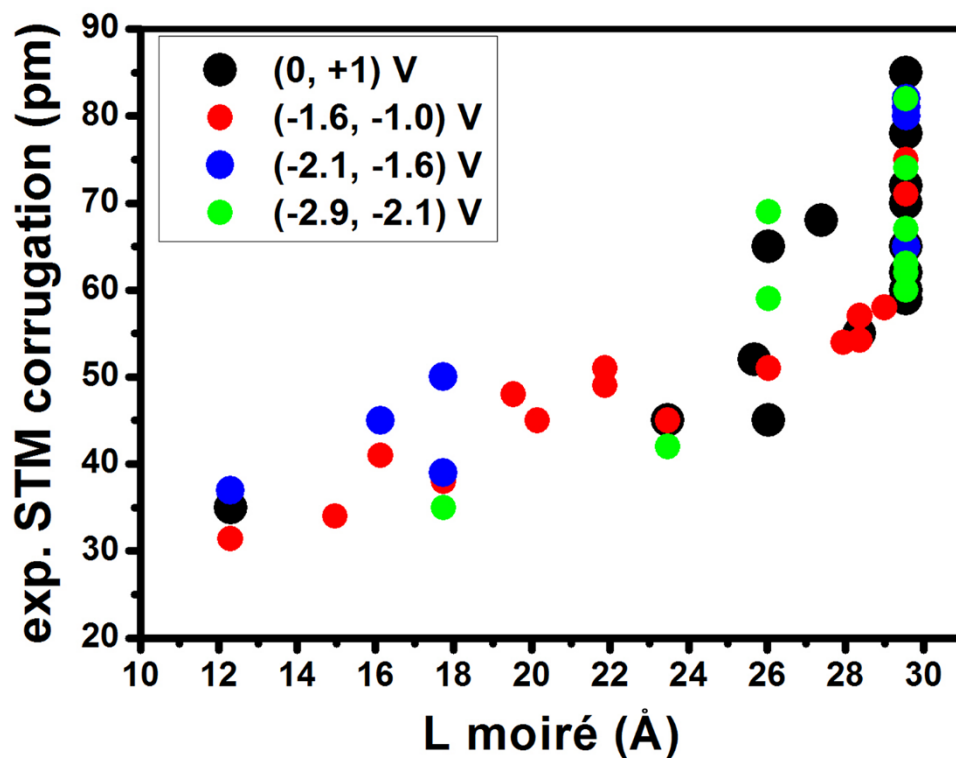


**Fig. S5.** Study of the moiré experimental corrugation variation with the bias voltage. Different moirés with different lattice parameters are plotted for four voltage ranges. No relevant dependency of the apparent corrugation with the voltage is observed. The apparent corrugation trend with the moiré lattice parameter is preserved in the four ranges.

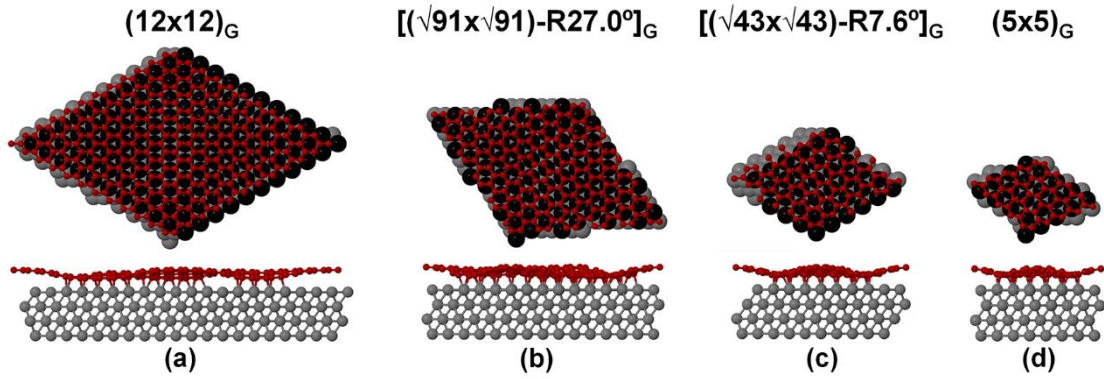


**Fig. S6.** G/Rh(111) moiré pattern ball-and-stick models of the four unit cells used in DFT simulations: (a)  $(12 \times 12)_G$ , or moiré 0 according to the notation in the main text, (b)  $[(\sqrt{91} \times \sqrt{91})\text{-R}27.0^\circ]_G$ , moiré 8, (c)  $[(\sqrt{43} \times \sqrt{43})\text{-R}7.6^\circ]_G$  or moiré 14 and (d)  $(5 \times 5)_G$  or moiré 16. C atoms are shown in red and Rh atoms in gray except in the top views where the atoms in the uppermost layer of Rh are shown in black.

#### 4. G/Rh moiré patterns used in the DFT simulations

##### 4.1 Computational details.

We have simulated four of the seventeen moiré patterns found in the STM experiments on the G/Rh(111) system. The ball-and-stick models of the unit cells used in the simulations are shown in fig. S6. In all of the cases, we have represented the metal by a four-layer rhodium slab. Atoms belonging to the two bottom layers were kept fixed while all of the rest were allowed to relax to find their equilibrium positions until forces upon atoms were less than 0.01 eV/Å. Our C-C equilibrium distance for a free-standing graphene was 1.4248 Å and the reticular parameter obtained for rhodium 3.7729 Å. We have used  $\Gamma$ -centered Monkhorst-Pack grids<sup>32, 42</sup> to sample the reciprocal space according to the size of the unit cell (see table S1). Tersoff-Hamann images and NEGF STM profiles are calculated with finer reciprocal space grids (table S1).

| MOIRÉ | k-points (relax.) | k-points (STM) | Rh atoms | C atoms | Side Length (Å) |
|-------|-------------------|----------------|----------|---------|-----------------|
| 0     | Gamma             | 7×7×1          | 484      | 288     | 29.66 / 29.56   |
| 8     | 2×2×1             | 7×7×1          | 304      | 182     | 23.50 / 23.42   |
| 14    | 2×2×1             | 11×11×1        | 144      | 86      | 16.17 / 16.12   |
| 16    | 5×5×1             | 15×15×1        | 84       | 50      | 12.35 / 12.31   |

**Table S1:** Input data for the DFT simulations of the four moiré patterns: Monkhorst-Pack grids used in atomic relaxations and STM calculations, total number of Rh and C atoms per cell, and the two side lengths (the length of one of the unit cell vectors) corresponding to the two criteria used to build the unit cells (see text).

## 4.2 Construction of the moiré patterns: experimental strains vs experimental lattice parameters.

In our simulations we have to set the size of the unit cell in order to mimic the commensurate relation between the graphene and rhodium individual cells. In the experiments, it is assumed that rhodium keeps unaltered while graphene is strained to avoid the mismatch. Since experimental lattice parameters are very close to those obtained in DFT simulations, a reasonable choice would be to take directly these values. We named this choice as *experimental lengths*. However, the slight difference between experimental and theoretical lattice parameters leads to inappropriate values of the strain in the graphene sheet. As the strain induced in the graphene is playing a role in the layer corrugation we decided to fit the length of the unit cells to directly reproduce the experimental value of the G-strain. This criterion, named as *experimental strains*, is the one we have used as reference in this work. The structures used for the STM calculations (and characterized in Table S2) and the energy contributions in Table 2 in the main text correspond to this criterion.

In order to ensure that our conclusions do not depend on this choice, we have carried out the simulations with both criteria. This study offers also the possibility to further study the influence of strain on the corrugation values, as the only difference that results from the application of these criteria is the side length, the length of one of the lattice vectors defining the unit cell. The values of the side length are included in the last column of table S1, where the first value corresponds to *experimental strains* criterion and the second one to *experimental lengths*.

| MOIRÉ | $z_{av}$ | $\sigma_z$ | $z_{min}$ | $z_{max}$ | $C_G$ | $C_{Rh}$ | Strain |
|-------|----------|------------|-----------|-----------|-------|----------|--------|
|       | (Å)      |            |           |           |       |          | (%)    |
| 0     | 2.49     | 0.39       | 1.94      | 3.15      | 1.21  | 0.16     | 0.15   |
| 8     | 2.50     | 0.39       | 1.96      | 3.22      | 1.26  | 0.14     | -0.16  |
| 14    | 2.49     | 0.35       | 2.07      | 3.14      | 1.07  | 0.11     | -0.04  |
| 16    | 2.39     | 0.30       | 2.01      | 2.94      | 0.92  | 0.14     | 0.13   |

**Table S2:** Structural parameters (in Å) from the DFT simulations (using the *experimental strains*).  $z_{av}$ ,  $z_{min}$  and  $z_{max}$  are the average, the minimum and maximum heights of the graphene with respect the Rh(111) surface and  $\sigma_z$  is the standard deviation of the C atoms heights. Notice that  $z_{min}$  and  $z_{av}$  are the adsorption distance and the average adsorption distance.  $C_G$  and  $C_{Rh}$  are the corrugations of graphene and the uppermost layer of the Rh(111) surface respectively.

Table S2 shows structural parameters obtained after the atomic relaxation of the four moiré patterns simulated using the *experimental strains*.  $z_{av}$  is the average C height with respect to the Rh(111) surface. Its value is the same,  $\sim 2.5$  Å, for the three largest moiré patterns and lower,  $\sim 2.4$  Å, for the smallest moiré. This tendency is also found in the standard deviation. However, results do not show any tendency with the system size for the lowest C heights,  $z_{min}$ . Regarding the C atoms placed on the highest positions, they are closer to the surface for the moiré 16, while the maximum value is found in moiré 8. This is reflected on the G layer corrugation that grows from moiré 16 to moiré 8 and slightly decays for the largest moiré (0). As we have pointed out, the Rh surface stays almost unperturbed, showing no significant corrugation in the uppermost layer ( $C_{Rh} \approx 0.2$  Å). The strain induced in the graphene layer is shown in the last column of the table. All values are very low (less than 0.2%), with both positive (stretching) and negative (compressive) character that does not seem to be correlated with system size. Although the system size and the G-Rh interaction are the most relevant parameters defining the final corrugation we will show below that the strain is also playing a role on the buckling of the G.

| MOIRÉ | $z_{av}$ | $\sigma_z$ | $z_{min}$ | $z_{max}$ | $C_G$ | $C_{Rh}$ | Strain |
|-------|----------|------------|-----------|-----------|-------|----------|--------|
|       | (Å)      |            |           |           |       |          | (%)    |
| 0     | 2.52     | 0.41       | 1.93      | 3.18      | 1.24  | 0.16     | -0.19  |
| 8     | 2.55     | 0.41       | 1.95      | 3.27      | 1.32  | 0.14     | -0.50  |
| 14    | 2.51     | 0.37       | 2.05      | 3.19      | 1.14  | 0.11     | -0.38  |
| 16    | 2.41     | 0.31       | 2.01      | 2.97      | 0.97  | 0.15     | -0.21  |

**Table S3.** Structural parameters (in Å) from the DFT simulations (using the *experimental lengths*):  $z_{av}$ ,  $z_{min}$  and  $z_{max}$  are the average, the minimum and maximum heights of the graphene with respect to the Rh(111) surface.  $\sigma_z$  is the standard deviation of the C atoms heights. Notice that  $z_{min}$  and  $z_{av}$  are the adsorption distance and the average adsorption distances.  $C_G$  and  $C_{Rh}$  are the corrugations of graphene and the uppermost layer of Rh(111) surface respectively.

The *experimental lengths* criterion yields unit cells larger than those provided by the *experimental strains*, i.e., the graphene is stretched with respect to the calculations shown above (see the different strains for the same moiré patterns on tables S2 and S3). On table S3 we show the structural parameters obtained with simulations using the *experimental lengths* criterion. The corrugation of the G layer shows the same behaviour with system size explained above but the values are always slightly larger. This is due to the fact that

compressive strains promote the corrugation of the graphene sheet while stretching causes the contrary effect. Apart from this, we have not found relevant differences between the two sets of data and the general tendencies are the same.

We have analyzed the stability of the moiré patterns on G/Rh(111) calculating the energy balance between interaction and deformation energies. We define the adsorption energy,  $E_{ad}$ , as the difference between the energy of the whole system and the energy of ground state of the isolated subsystems, both graphene and rhodium. The interaction energy,  $E_{int}$ , just measures the energy yielded directly by the G-Rh coupling, i.e. it does not take into account the energies needed to distort graphene and rhodium, which we define as the deformation energies,  $\Delta E(G)$  and  $\Delta E(Rh)$ . So according to this, interaction and adsorption energies are related as follows:  $E_{ad} = E_{int} + \Delta E(G) + \Delta E(Rh)$ . Notice that deformation energies  $\Delta E$  have two terms  $\Delta E = E_{strain} + E_{cor}$ . The first term is related with the change in the reticular parameter, i.e. the strain energy, and the second one represents the energy needed to corrugate the G layer or the Rh(111) surface.

| Energy (meV/C atom)                         | moiré 0     | moiré 8     | moiré 14    | moiré 16    |
|---|-------------|-------------|-------------|-------------|
| <b><math>E_{ad}</math></b>                  | <b>-137</b> | <b>-109</b> | <b>-134</b> | <b>-140</b> |
| $\Delta E(G)$ ( $E_{strain}$ , $E_{cor}$ )  | 17 (<1, 17) | 19 (<1, 19) | 25 (<1, 25) | 40 (<1, 40) |
| $\Delta E(Rh)$ ( $E_{strain}$ , $E_{cor}$ ) | 19 (15, 4)  | 20 (15, 5)  | 19 (15, 4)  | 22 (15, 7)  |
| $E_{int}$                                   | -173        | -147        | -178        | -202        |

**Table S4.** Some important energies of the DFT simulations using the *experimental lengths* criterion:  $\Delta E(G)$  and  $\Delta E(Rh)$  are the energies needed to corrugate ( $E_{cor}$ ) and stretch or compress ( $E_{strain}$ ) the G sheet and the Rh surface respectively,  $E_{ad}$  is the difference in energies between the whole system and the clean and isolated subsystems, G and Rh, and  $E_{int}$  is the interaction energy between the metal and the graphene sheet calculated as the difference between the whole system and the distorted subsystems.

In the main text, we have shown (Table 2) and discussed the results yielded by the simulations with the *experimental strains*. On table S4 we present the results calculated with the *experimental lengths*. As expected, Rh deformation energies are smaller than those calculated with the *experimental strains* and, again, do not show important variations with system size. The values of the deformation energies of G and the interaction energy are also very similar with both criteria, leading to the same behaviour in the adsorption energy. Thus, our conclusions regarding the structure and stability of

the different moirés and the variation with system size are robust and do not depend on the criteria used to build the moiré patterns.

Finally, in order to learn more about the influence of strain in corrugation we have also analyzed in detail the behaviour of moiré 8 carrying out extra calculations. In our simulations, no matter the criterion used, this moiré pattern always shows the maximum compressive strain (-0.50% / -0.16% with the *experimental strains/lengths* criterion) and yields the highest G corrugation, 1.32 Å / 1.26 Å respectively. These results already indicate a reduction of the corrugation induced by a stretching strain. We have stretched the layer even further and found, for a strain of +0.08% -closer to the strain of moiré 0 with the *experimental strain* criterion-, that the corrugation is reduced to 1.21 Å, just the same of moiré 0 with +0.15% strain. This analysis confirms that the G corrugation is already saturated with respect to the system size for the lengths corresponding to the moiré 8 and that the variations observed are related to the character of the strain (compressive/stretching) induced on the G layer.

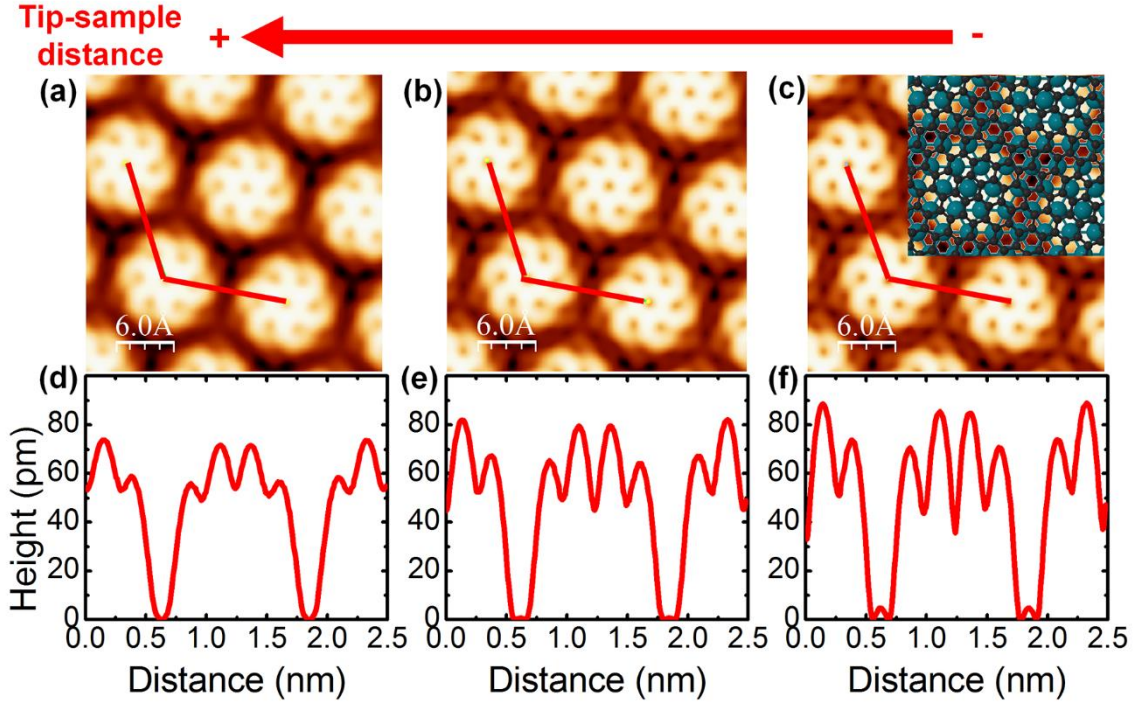


**Fig. S7.** Tersoff-Hamann images of the moiré 16 for  $V_s = -1$  V and different values of constant LDOS isosurfaces of  $1.56 \times 10^{-6} \text{ \AA}^{-3}$  (a),  $6.25 \times 10^{-6} \text{ \AA}^{-3}$  (b) and  $1.25 \times 10^{-5} \text{ \AA}^{-3}$  (c). Each image is presented with height profiles along the red path in the image (d-f). Notice how bright zones correspond with high regions of the moiré patterns with C atoms on hollow positions while dark zones correspond to low regions with C atoms on top positions. The inset in (c) shows a ball-and-stick model of graphene and the uppermost Rh(111) layer.

## 5. Apparent corrugation of graphene on Rh(111) in STM simulations

We have calculated theoretical STM images using the Tersoff-Hamann approximation<sup>35</sup> of the moiré patterns of the G/Rh system. As an illustrative example we show in fig. S7 (a-c) the Tersoff-Hamann images obtained with VASP by integration of the LDOS in the same energy window of -1 eV used in the NEGF calculations discussed in the main text, and treated with the WSXM software,<sup>41</sup> of the  $(5 \times 5)_G$  moiré pattern for different isosurface values, corresponding to a constant integrated LDOS of  $1.56 \times 10^{-6} \text{ \AA}^{-3}$ ,  $6.25 \times 10^{-6} \text{ \AA}^{-3}$  and  $12.5 \times 10^{-6} \text{ \AA}^{-3}$ . On fig. S7d-f we show the line profiles along the red path displayed in Fig. S7a-c. The apparent corrugations increase from 70 to 90 pm with the isosurface value. They are a little bit smaller than the geometrical value, 92 pm, obtained with DFT and still far from the apparent corrugation measured on the STM experiments, 30 pm for this moiré. In order to compare the apparent corrugation calculated with this technique with the experimental one we have chosen an isosurface value of  $1.56 \times 10^{-6} \text{ \AA}^{-3}$  (Fig. S7a and d), one of the smaller values in which atomic resolution is found in the

highest parts of the moiré pattern but not on the dark zones, similar to the situation in the experimental data. If we move to even lower isosurface values, the apparent corrugation can decrease down to ~50 pm but the atomic resolution is completely lost. In Fig. S8 we compare the apparent corrugation obtained with the Tersoff-Hamann approximation (green pentagons) as a function of the system size with the geometric G buckling (red circles) and the experimental measurements (black squares). The Tersoff-Hamann apparent corrugation is always slightly smaller than the real deformation and much larger than the experimental one.

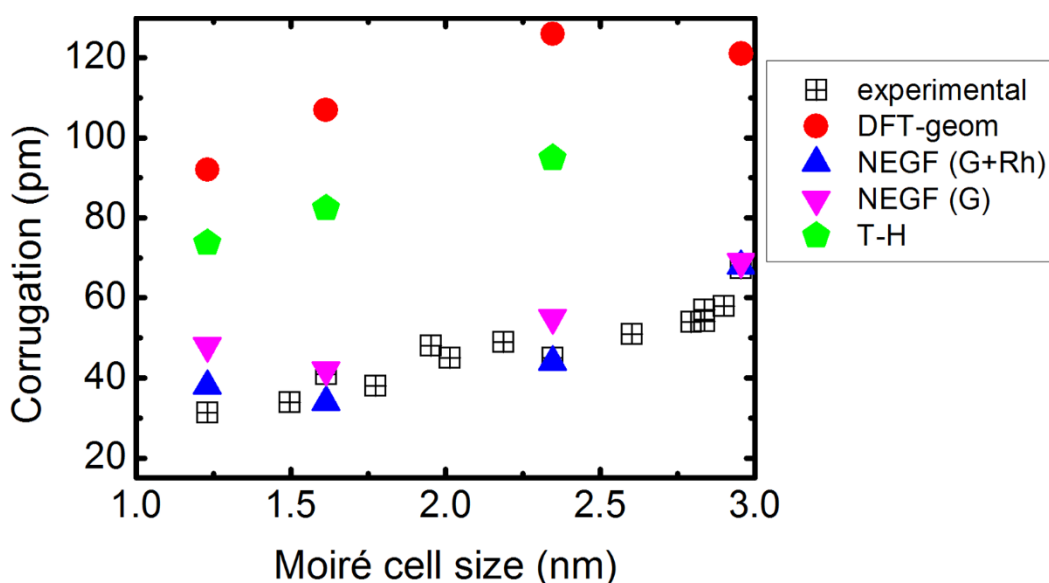


**Fig. S8.** Comparison between the corrugation values obtained in DFT simulations (red circles) with the STM apparent corrugation. The apparent corrugation values obtained with Tersoff-Hamann approximation (green pentagons) are lower than the geometric values but still far from the experimental measurements (black squares). However, when NEGF formalism is used there is a clear agreement between theoretical and experimental data. Apparent corrugations with the tunnelling current calculated between the tip and only the carbons atoms in the graphene (pink down triangles) and between the tip and the graphene and the first Rh layer (blue up triangles) are shown.

Since Tersoff-Hamann approximation fails to describe this strong-interacting system we employ a formalism based on Non-Equilibrium Green's Functions (NEGF)<sup>25</sup> to calculate the tunnelling current. With this technique the electronic current between each atom of the tip model and the sample is accurately calculated. In this case we simulated the tip with a single metal atom with a  $d_{z^2}$ -orbital, apex successfully used in previous works on G on Pt.<sup>11,36</sup> Results, tunnelling to both G and the first Rh layer, are shown in Fig. S8 (blue up triangles). Now the agreement with the experiment is excellent. We can study

the effect of the metal on the apparent corrugation allowing the current on the STM simulation to go only through the G layer (pink down triangles). In this case, the corrugation is slightly larger but still close to the experimental values. The reduction of the STM apparent corrugation with respect to the geometrical values mainly comes from the spatial distribution of the tip-surface current which is well described using the NEGF formalism but not with the Tersoff-Hamann approach. In carbon based materials, not only the surface atom closer to the outermost tip apex atoms contribute significantly to the tip-sample current<sup>28</sup>. Neighboring carbons also carry significant electronic currents so the curvature of the layers will be always reduced in the STM images. Therefore, the nearly linear growth of the STM apparent corrugation with the system size found for the graphene on Rh is a result of both the increase of the real geometric buckling and the reduction of the average curvature of the G layer with the moiré pattern length.

## 6. Complete list of references

1. A. K. Geim, *Science*, 2009, **324**, 1530-1534.
2. S. Bae, H. Kim, Y. Lee, X. F. Xu, J. S. Park, Y. Zheng, J. Balakrishnan, T. Lei, H. R. Kim, Y. I. Song, Y. J. Kim, K. S. Kim, B. Ozyilmaz, J. H. Ahn, B. H. Hong and S. Iijima, *Nat. Nanotechnol.*, 2010, **5**, 574-578.
3. H. Yang, J. Heo, S. Park, H. J. Song, D. H. Seo, K. E. Byun, P. Kim, I. Yoo, H. J. Chung and K. Kim, *Science*, 2012, **336**, 1140-1143.
4. K. C. Yung, W. M. Wu, M. P. Pierpoint and F. V. Kusmartsev, *Contemp. Phys.*, 2013, **54**, 233-251.
5. X. S. Li, W. W. Cai, J. H. An, S. Kim, J. Nah, D. X. Yang, R. Piner, A. Velamakanni, I. Jung, E. Tutuc, S. K. Banerjee, L. Colombo and R. S. Ruoff, *Science*, 2009, **324**, 1312-1314.
6. A. K. Geim and K. S. Novoselov, *Nat. Mater.*, 2007, **6**, 183-191.
7. A. B. Preobrajenski, M. L. Ng, A. S. Vinogradov and N. Martensson, *Phys. Rev. B*, 2008, **78**, 073401.
8. A. L. V. de Parga, F. Calleja, B. Borca, M. C. G. Passeggi, J. J. Hinarejos, F. Guinea and R. Miranda, *Phys. Rev. Lett.*, 2008, **100**, 056807.
9. G. Giovannetti, P. A. Khomyakov, G. Brocks, V. M. Karpan, J. van den Brink and P. J. Kelly, *Phys. Rev. Lett.*, 2008, **101**, 026803.
10. M. Batzill, *Surf. Sci. Rep.*, 2012, **67**, 83-115.
11. M. M. Ugeda, D. Fernandez-Torre, I. Brihuega, P. Pou, A. J. Martinez-Galera, R. Perez and J. M. Gomez-Rodriguez, *Phys. Rev. Lett.*, 2011, **107**, 116803.
12. I. Pletikosic, M. Kralj, P. Pervan, R. Brako, J. Coraux, A. T. N'Diaye, C. Busse and T. Michely, *Phys. Rev. Lett.*, 2009, **102**, 056808.
13. A. J. Martinez-Galera, I. Brihuega and J. M. Gomez-Rodriguez, *Nano Lett.*, 2011, **11**, 3576-3580.
14. P. Sutter, J. T. Sadowski and E. Sutter, *Phys. Rev. B*, 2009, **80**, 245411.
15. B. Borca, S. Barja, M. Garnica, M. Minniti, A. Politano, J. M. Rodriguez-Garcia, J. J. Hinarejos, D. Farias, A. L. V. de Parga and R. Miranda, *New J. Phys.*, 2010, **12**, 093018.
16. E. Miniussi, M. Pozzo, A. Baraldi, E. Vesselli, R. R. Zhan, G. Comelli, T. O. Montes, M. A. Nino, A. Locatelli, S. Lizzit and D. Alfe, *Phys. Rev. Lett.*, 2011, **106**, 216101.
17. B. Wang, M. Caffio, C. Bromley, H. Fruchtl and R. Schaub, *ACS Nano*, 2010, **4**, 5773-5782.
18. P. Merino, M. Svec, A. L. Pinardi, G. Otero and J. A. Martin-Gago, *ACS Nano*, 2011, **5**, 5627-5634.
19. A. T. N'Diaye, R. van Gastel, A. J. Martinez-Galera, J. Coraux, H. Hattab, D. Wall, F. J. M. zu Heringdorf, M. Horn-von Hoegen, J. M. Gomez-Rodriguez, B. Poelsema, C. Busse and T. Michely, *New J. Phys.*, 2009, **11**, 113056.
20. A. J. Martinez-Galera and J. M. Gomez-Rodriguez, *J. Phys. Chem. C*, 2011, **115**, 23036-23042.
21. A. Martín-Recio, A. J. Martínez-Galera and J. M. Gómez-Rodríguez, *J. Phys. Chem. C*, 2015, **119**, 401-406.
22. D. Stradi, S. Barja, C. Diaz, M. Garnica, B. Borca, J. J. Hinarejos, D. Sanchez-Portal, M. Alcamí, A. Arnau, A. L. V. de Parga, R. Miranda and F. Martín, *Phys. Rev. Lett.*, 2011, **106**, 186102.
23. M. Iannuzzi and J. Hutter, *Surf. Sci.*, 2011, **605**, 1360-1368.

24. E. N. Voloshina, Y. S. Dedkov, S. Torbrugge, A. Thissen and M. Fonin, *Appl. Phys. Lett.*, 2012, **100**, 241606.
25. J. M. Blanco, F. Flores and R. Perez, *Prog. Surf. Sci.*, 2006, **81**, 403-443.
26. R. Cortes, D. P. Acharya, C. V. Ciobanu, E. Sutter and P. Sutter, *J. Phys. Chem. C*, 2013, **117**, 20675-20680.
27. S. K. Hamalainen, M. P. Boneschanscher, P. H. Jacobse, I. Swart, K. Pussi, W. Moritz, J. Lahtinen, P. Liljeroth and J. Sainio, *Phys. Rev. B*, 2013, **88**, 201406.
28. M. Ondracek, P. Pou, V. Rozsival, C. Gonzalez, P. Jelinek and R. Perez, *Phys. Rev. Lett.*, 2011, **106**, 176101.
29. G. Kresse and J. Furthmuller, *Phys. Rev. B*, 1996, **54**, 11169-11186.
30. J. P. Perdew, K. Burke and M. Ernzerhof, *Phys. Rev. Lett.*, 1996, **77**, 3865-3868.
31. S. Grimme, *J. Comput. Chem.*, 2006, **27**, 1787-1799.
32. P. E. Blochl, *Phys. Rev. B*, 1994, **50**, 17953-17979.
33. G. Kresse and D. Joubert, *Phys. Rev. B*, 1999, **59**, 1758-1775.
34. C. Lee, X. D. Wei, J. W. Kysar and J. Hone, *Science*, 2008, **321**, 385-388.
35. J. Tersoff and D. R. Hamann, *Phys. Rev. Lett.*, 1983, **50**, 1998-2001.
36. P. Merino, L. Rodrigo, A. L. Pinardi, J. Mendez, M. F. Lopez, P. Pou, R. Perez and J. A. M. Gago, *ACS Nano*, 2014, **8**, 3590-3596.
37. O. Custance, S. Brochard, I. Brihuega, E. Artacho, J. M. Soler, A. M. Baro and J. M. Gomez-Rodriguez, *Phys. Rev. B*, 2003, **67**, 235410.
38. A. J. Martinez-Galera and J. M. Gomez-Rodriguez, *J. Phys. Chem. C*, 2011, **115**, 11089-11094.
39. MaTeck GmbH, [www.mateck.de](http://www.mateck.de).
40. SPL, [www.spl.eu](http://www.spl.eu).
41. I. Horcas, R. Fernandez, J. M. Gomez-Rodriguez, J. Colchero, J. Gomez-Herrero and A. M. Baro, *Rev. Sci. Instrum.*, 2007, **78**, 013705.
42. H. J. Monkhorst and J. D. Pack, *Phys. Rev. B*, 1976, **13**, 5188-5192.
43. B. Wang and M. L. Bocquet, *J. Phys. Chem. Lett.*, 2011, **2**, 2341-2345.
44. J. Klimes, D. R. Bowler and A. Michaelides, *J. Phys.: Condens. Matter*, 2010, **22**, 022201.
45. T. Ozaki, *Phys. Rev. B*, 2003, **67**, 155108.
46. T. Ozaki and H. Kino, *Phys. Rev. B*, 2004, **69**, 195113.